Goniometric and Polarized Imaging Spectroscopic Lab Measurements of Spacecraft Materials

Chris H. Lee, Charles M. Bachmann

Rochester Institute of Technology, Chester F. Carlson Center for Imaging Science

Patrick Seitzer

University of Michigan, Department of Astronomy

Heather M. Cowardin

NASA Johnson Space Center, Orbital Debris Program Office

ABSTRACT

To better characterize the spectral response of common spacecraft materials, the following laboratory measurements are presented to support the Space Situational Awareness community in the analysis of remotely sensed observational data. Of interest is classifying material reflective properties using directional reflectance spectroscopy and spatially resolved polarized imaging spectroscopy, allowing laboratory data to be applicable to ground-based optical telescope observations. The team acquired a typical CubeSat solar panel and a sample of multi-layer insulation (MLI) commonly used on spacecraft for initial measurements. The directional spectral data were collected at the Goniometer of the Rochester Institute of Technology (GRIT) laboratory with a lab and field goniometer incorporating two Analytical Spectral Device (ASD) spectrometers, a small Labsphere integrating sphere also paired with an ASD spectrometer, and a Headwall micro-Hyperspec E-Series imaging spectrometer with an adjustable linear polarizer. The goniometer measures spectral bi-directional reflectance factor (BRF) data over a broad range from $350-2500$ nm at 1 nm spacing with 3 nm spectral resolution in the visible and near infrared and 8 nm in the shortwave infrared. With the same spectral capabilities, the integrating sphere measures hemispherical-directional reflectance (HDR) in a $45°$-nadir configuration. The Headwall imager covers a spectral range from $400-1000$ nm with 1.6 nm spectral resolution. Our initial BRF measurements show interference effects for both materials typically observed with thin films and high infrared reflectivity. In contrast, the interference effects are not present in the HDR measurements of the MLI likely due to the interference effects being averaged out over the reflecting hemisphere. Spatially resolved polarization ratio maps show variability across the materials due to the varying surface structure. We outline a plan for expanding our analysis to a broader range of materials to characterize their directional reflectance spectroscopy.

1. INTRODUCTION

Directional reflectance spectroscopy is a technique for characterizing the angular scattering or reflective properties of a material or physical medium as a function of the wavelength of light. Reflectance is a directional quantity, meaning that the measurement or observational geometries as well as the illumination geometries directly impact the measured spectrum of the target. In Earth remote sensing contexts, incorporating angular scattering characteristics of natural media for radiative transfer models can provide better constraints for remote sensing retrievals compared to that of a single measurement geometry [1, 2]. For space situational awareness (SSA) or space domain awareness (SDA) applications, quantifying the directional reflectance characteristics of various spacecraft material surfaces is critical for accurate photometric or radiometric modeling of remotely-sensed resident space object (RSO) signatures [3, 4]. There are various measures of angular reflectance, two of which used for this analysis are the **bi-directional reflectance factor (BRF)** and the **hemispherical-directional reflectance (HDR)** [5, 6].

The BRF is a dimensionless quantity that is measured and calculated as a ratio of the signal from a surface with a given observational geometry normalized by the signal from a diffusely reflecting, or Lambertian, panel in the same observing geometry. That is,
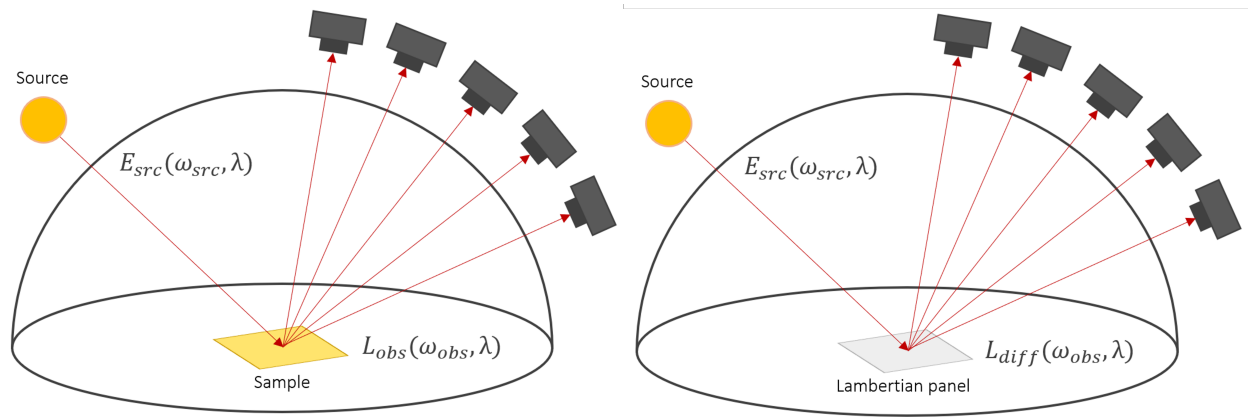
Fig. 1: A diagram of the BRF measurement geometries involving a sample and a Lambertian panel. The source and observer angular directions are denoted by ω_{src} and ω_{obs}. The source irradiance, measured sample radiance, and measured diffuse panel radiance are denoted by E_{src}, L_{obs}, and L_{diff}. λ denotes the wavelength of light.
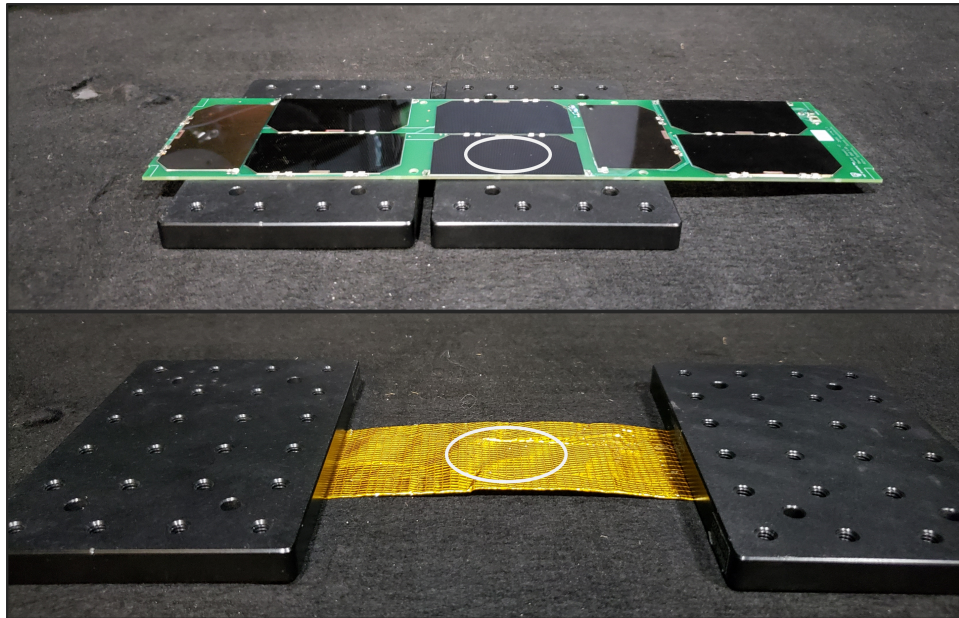

Fig. 2: (Top) The CubeSat solar panel with integrated BTJM photovoltaic cells used for our analyses. (Bottom) The multi-layer insulation sample used for our analyses. The encircled region approximately shows the area measured by GRIT-T's field of view for BRF data and the integrating sphere for HDR data for the MLI.

$$\rho_{BRF}(\omega_{src}; \omega_{obs}, \lambda) = \frac{L_{obs}(\omega_{obs}, \lambda)}{L_{diff}(\omega_{obs}, \lambda)} \tag{1}$$

for BRF ρ_{BRF}, angular direction of source from target ω_{src}, angular direction of target to observer ω_{obs}, wavelength of light λ, measured radiance of target at observer L_{obs}, and measured radiance of diffuse Lambertian panel L_{diff}. For a given illumination geometry, the ideal Lambertian surface should produce the same radiance in all directions. In practice, however, the reference surface is not perfectly Lambertian, but departure from this assumption can be modeled [7] and the effects mitigated, minimizing the number of repeated measurements needed for the reference surface. The BRF quantifies the reflective properties of a surface or medium as a function of angles. Fig. 1 shows a diagram of the BRF measurement geometries. The HDR is the directional reflectance of a sample that is illuminated under a uniform hemisphere. That is,

$$\rho_{HDR}(\lambda) = \int_{2\pi} \rho_{BRDF}(\omega_{src}; \omega_{obs}, \lambda) d\Omega_{src} = \int_{2\pi} \frac{L_{obs}(\omega_{obs}, \lambda)}{E_{src}(\omega_{src}, \lambda)} d\Omega_{src} \tag{2}$$

for bi-directional reflectance distribution function (BRDF) ρ_{BRDF}, source irradiance E_{src}, and differential solid angle from illumination $d\Omega_{src}$. In our analysis, we measure the BRF of our samples using a goniometer [8] and the HDR using a small integrating sphere.

In addition to these angular reflectance quantities, we also measure the polarimetry of our samples using an imaging spectrometer with an adjustable linear polarizer. Polarimetry is the technique of measuring and quantifying polarized light from a target, which can further be used for material and target characterization [9, 10]. In our analysis, we measure and calculate the spectral polarization ratio between 0° and 90° polarization states as

$$P(\lambda) = \frac{R_{0°}(\lambda) - R_{90°}(\lambda)}{R_{0°}(\lambda) + R_{90°}(\lambda)} \tag{3}$$

for polarization ratio spectrum $P(\lambda)$, reflectance spectrum at 0° polarization $R_{0°}(\lambda)$, and reflectance spectrum at 90° polarization $R_{90°}(\lambda)$.

2. SAMPLES AND INSTRUMENTATION

The two samples for our analysis were (1) a piece of multi-layer insulation (MLI) with an aluminized Kapton surface and (2) a CubeSat solar panel with integrated Emcore BTJM photovoltaic cells. Fig. 2 shows the samples with their measurement regions indicated by the circles. Various instruments were used for measurements of our CubeSat solar panel and MLI sample. These included: (1) the Goniometer of the Rochester Institute of Technology-Two (GRIT-T) [8], which incorporates Analytical Spectral Device (ASD) spectrometers for spectral BRF measurements, (2) a small Labsphere integrating sphere also paired with an ASD spectrometer for spectral HDR measurements, and (3) a Headwall micro-Hyperspec E-Series imaging spectrometer with an adjustable linear polarizer for imaging spectroscopic polarimetry. Images of the instruments are shown in Fig. 3.

The BRFs of the samples were measured at three illumination zenith angles of 15°, 30°, and 45°. The scan pattern of the MLI was set to 20° steps in azimuth in a full circle around the hemisphere and 7.5° steps in zenith from 0° at nadir down to 52.5°. The scan pattern of the photovoltaic cell was split into two scans due to its highly specular nature comprised of a coarse scan around the hemisphere excluding points at specular region and a high resolution scan at and around the specular region. Excluding a small window around the specular region, the coarse hemispherical scan was set to 45° steps in azimuth in a full circle around the hemisphere and 10.5° steps in zenith from 0° at nadir down to 52.5°. The high resolution specular scan was set to a small ±5° window in both azimuth and zenith at the specular point in ±2.5° steps.

2.1 The Goniometer of the Rochester Institute of Technology-Two

GRIT-T is the second generation state-of-the-art field and laboratory goniometric system paired with two Analytical Spectral Device (ASD) spectrometers [8, 11, 12, 13, 14, 15, 16, 17]. The spectral range of the ASDs are from 350 nm
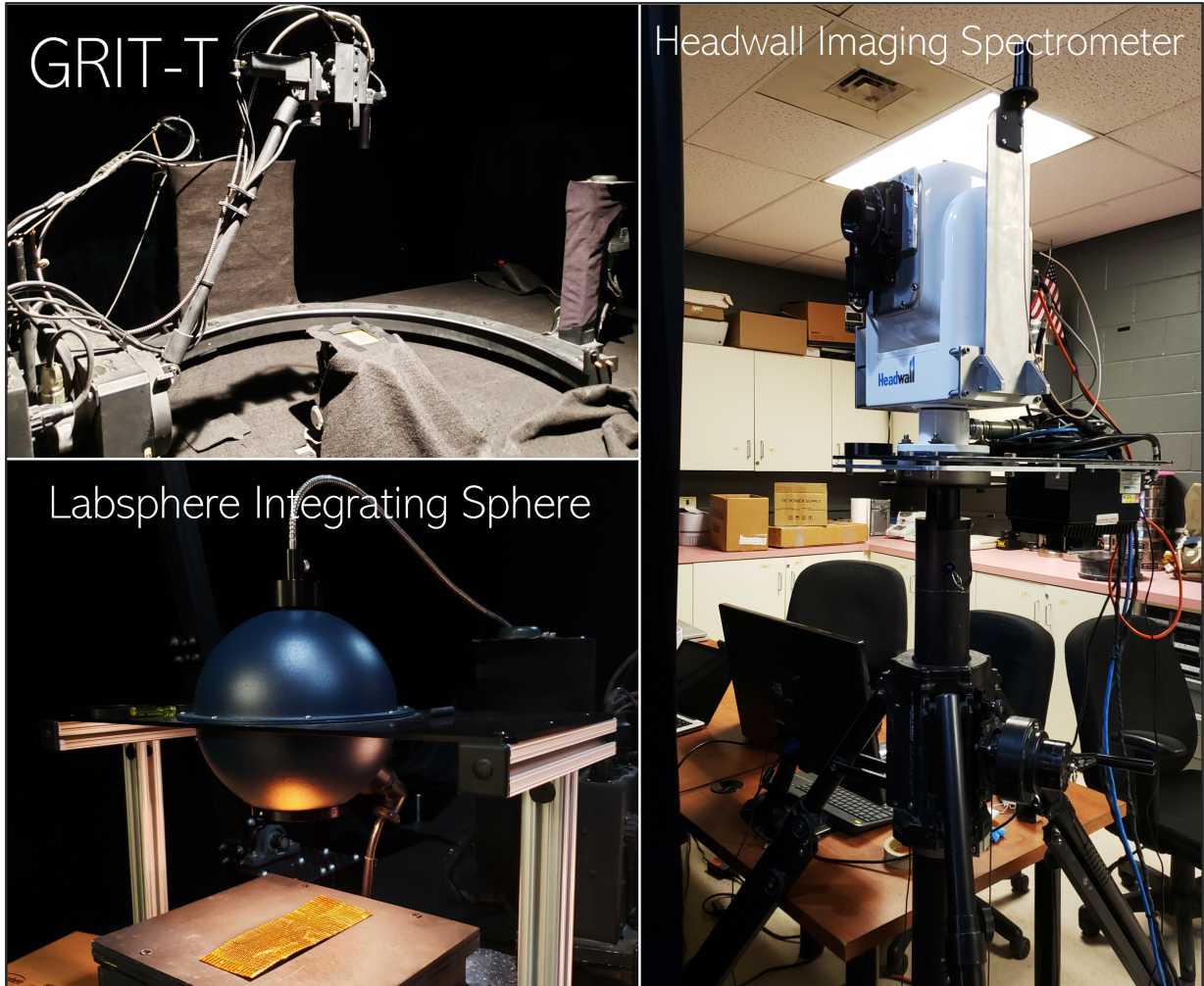
Fig. 3: The main instrumentation for our analyses is shown. (Top left) The Goniometer of the Rochester Institute of Technology-Two (GRIT-T) [8] used for spectral BRF measurements from 350 nm to 2500 nm with 1 nm resolution. (Bottom left) A small Labsphere integrating sphere for HDR measurements from 350 nm to 2500 nm with 1 nm resolution. (Right) The Headwall micro-HE imaging spectrometer with an adjustable linear polarizer for polarized imaging spectroscopy from 400 nm to 1000 nm with 1.6 nm resolution.

to 2500 nm at 1 nm steps with 3 nm spectral resolution in the visible and near-infrared and 8 nm in the shortwave infrared. In a laboratory setting, one of the ASDs were used, where the fiber optic cable connected to the ASD is run along the length of the goniometer's arm and affixed in the head socket. For this analysis, we used a 3° fore-optic for a narrower field of view due to our smaller sample sizes. Our samples were placed at the center of the scanning hemisphere, and a laser distance meter integrated into the goniometer head precisely measured the height of the samples. Our scan patterns were set in the goniometer control software, and the samples were illuminated using an external tungsten-halogen light source that is mounted on a motorized arm above the goniometer. GRIT-T then sequentially scanned the hemisphere according to the set pattern one point at a time. Once the sample hemisphere had been scanned, the sample was swapped out with a 99% reflectance Spectralon panel, and the spectrum of the panel was measured at nadir.

The spectra from the hemispherical scan of the sample and the Spectralon panel were recorded in digital numbers, which were converted to calibrated radiance using ViewSpecPro with the most recent ASD calibration files. The radiance values of the sample were then converted into reflectance values by dividing the calibrated spectra of each sample measurement by the panel spectra with the Levesque-Dissanska non-Lambertian panel correction [7]. These intermediate spectra were additionally multiplied by the scaling factors of the directional-hemispherical reflectance of the panel (measured by Labsphere) itself to account for the fact that the Spectralon panels are not perfect reflectors. The resulting data products from this processing chain are the spectral BRFs.

2.2 The Labsphere Integrating Sphere

A small Labsphere integrating sphere was used for HDR measurements of our samples. The inner layer of the integrating sphere is coated with a uniform layer of highly reflective Spectraflect and consists of three main ports: (1) the exit port and aperture at the bottom of the sphere where the sample is placed, (2) the illumination port connected to a light source that is oriented 45° from the aperture that illuminates the integrating sphere, and (3) the measurement port at the top of the sphere where the bare fiber optic cable connected to an ASD can be inserted for spectral measurements.

In our HDR measurement process, we measure the spectra of eight diffuse Spectralon reflectance standard pucks at 2%, 5%, 10%, 20%, 40%, 60%, 80%, and 99% reflectance using the integrating sphere. Each puck is placed flush against the aperture and the spectra of every puck are recorded in digital numbers and converted into calibrated radiance using ViewSpecPro. The relationship between the measured radiance and the known reflectance at each wavelength was then determined using linear interpolation. The samples were then measured in the same manner by placing each sample flush against the aperture, and the measured radiances were then correlated to the reflectances in a manner similar to the empirical line method. For these measurements, the region of the MLI indicated in Fig. 2 for BRF measurements was also used for the HDR measurement, and the HDR of the back of the green solar panel board was also measured. HDR measurements from the photovoltaic cell are not presented as we are currently investigating the applicability of our integrating sphere configuration to highly specular surfaces.

2.3 The Headwall Photonics micro-HE Imaging Spectrometer

The Headwall imaging spectrometer is a hyperspectral pushbroom system housed in a General Dynamics pan-tilt unit, which generates the along-track dimension of the hyperspectral image (HSI) data [1]. The focal plane array is 1600 spatial pixels by 371 spectral pixels, and the along-track spatial dimension is limited by the angular range of the panning motor of the pan-tilt unit. The spectral range of the imaging spectrometer is from approximately 400 nm to 1000 nm with a spectral resolution of approximately 1.6 nm in 371 narrow bands. For this analysis, an adjustable linear polarizer was also affixed to the front aperture of the imaging spectrometer to take polarized HSI data of the samples. The Spectralon reflectance pucks and the spacecraft material samples were placed under the tungsten-halogen lamp and were illuminated from nadir. The polarizer was aligned to the 0° orientation using the control software and a polarized HSI was captured. The polarizer was then aligned to the 90° and the second polarized HSI was captured in the same configuration. The HSIs are similarly recorded in digital counts and were converted to radiance values using polarized calibration data that was measured with our Labsphere Helios integrating sphere [1] instead of the Headwall provided radiance calibration software, which is for unpolarized imagery. The polarized radiance spectra were then converted to polarized reflectance spectra by dividing the HSI cubes by the measured spectra of a Spectralon puck in the respective 0° and 90° orientations and multiplying the cubes with the known calibration coefficients of the pucks from LabSphere. The polarization ratio spectra were then calculated according to Eq. 3.
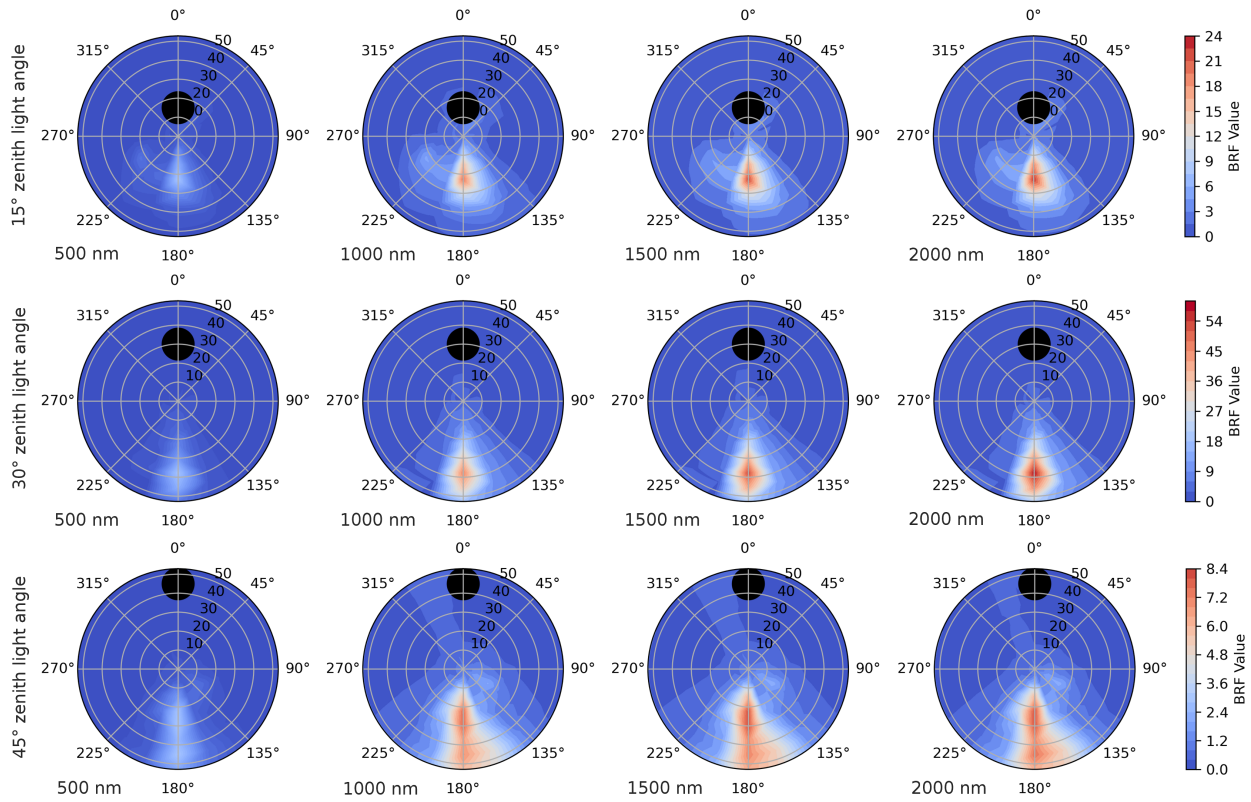
Fig. 4: BRFs of the MLI at three illumination zenith angles (from top row to bottom row) of 15°, 30°, and 45° at four individual wavelengths (from left-most column to right-most column) at 500 nm, 1000 nm, 1500 nm, and 2000 nm are shown. In the polar plots, the polar angle denotes the azimuthal angle and the radial distance from the center denotes the zenith angle on the observation hemisphere. The black circle denotes the backscattering direction where the light source, the goniometer head, and the sample are co-linear resulting in self-shadowing of the sample. The color axes are shared across the rows. For BRF values at angles in the plots that were not directly measured, the BRFs were linearly interpolated.

3.   RESULTS AND DISCUSSION

Results from the BRF measurements of the MLI and photovoltaic cell are shown for each of the three zenith illumination angles of 15°, 30°, and 45° in Figs. 4, 5, 6, and 7. BRFs at four individual wavelengths of 500 nm, 1000 nm, 1500 nm, and 2000 nm are shown in Figs. 4 and 6. Composite BRFs derived from three measured bands in the red, green and blue part of the spectrum and individual spectra around the specular regions are shown in Figs. 5 and 7. The BRFs are rendered as polar plots where the polar angle denotes the azimuthal angle and the radial distance denotes the zenith angle in the scan hemisphere. The black circle denotes the backscattering direction where the light source, the goniometer head, and the sample are co-linear resulting in self-shadowing of the sample.

In the BRFs for both samples, the illumination is primarily forward-reflected and concentrated in the vicinity of the specular region, but the peaks are offset from the specular angle as described below. Compared to the solar cell BRFs, the specular regions of the MLI exhibit a wider peak due to the more structured and diffusely scattering nature of the MLI surface. The solar cell BRFs show a concentrated peak around each of the specular points, where the width of the peak appears to be determined by the spot size of the lamp and the goniometer field of view. The winged appearance of the peak around the specular point for the solar cell BRF at 15° zenith illumination angle is likely an artifact resulting from interpolating the BRF plots for values between the actual measurements. We note that the MLI BRF at 30° illumination angle take maximal values close to 60 in the SWIR, although the maximal BRFs for 15° and 45° illumination angles are 25 and 8 in the SWIR, respectively. The overall values for the 45° MLI BRF appear lower
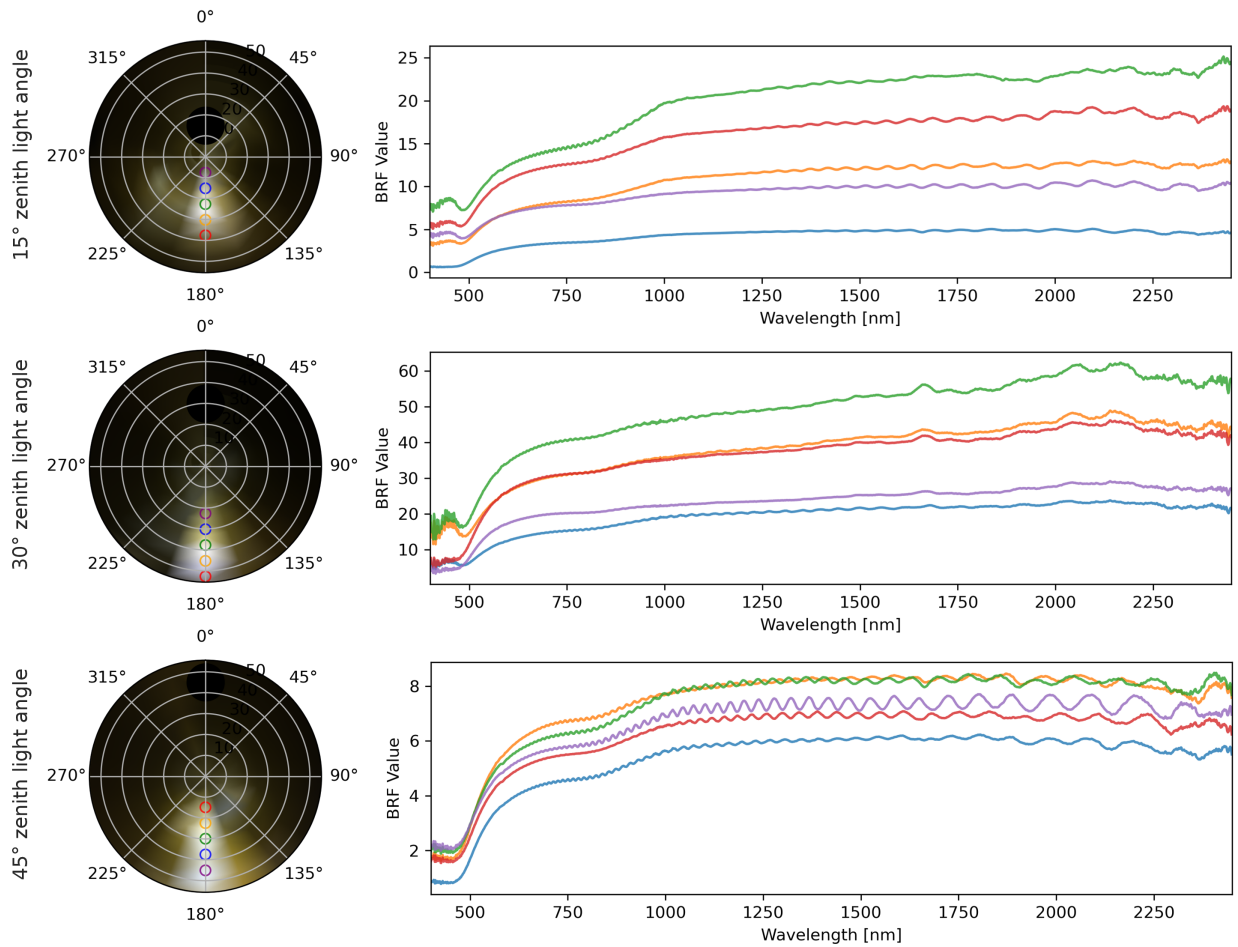
Fig. 5: (Left) Composite BRFs for a combination of single bands derived from the red, green, and blue portion of the measured spectrum of the MLI at the three illumination zenith angles are shown. (Right) Individual reflectance spectra around the specular regions are shown for which plots are color-coded to the circled regions in the RGB BRFs. The presence of a single-frequency interference effect shows that the MLI sample has a single substrate layer.
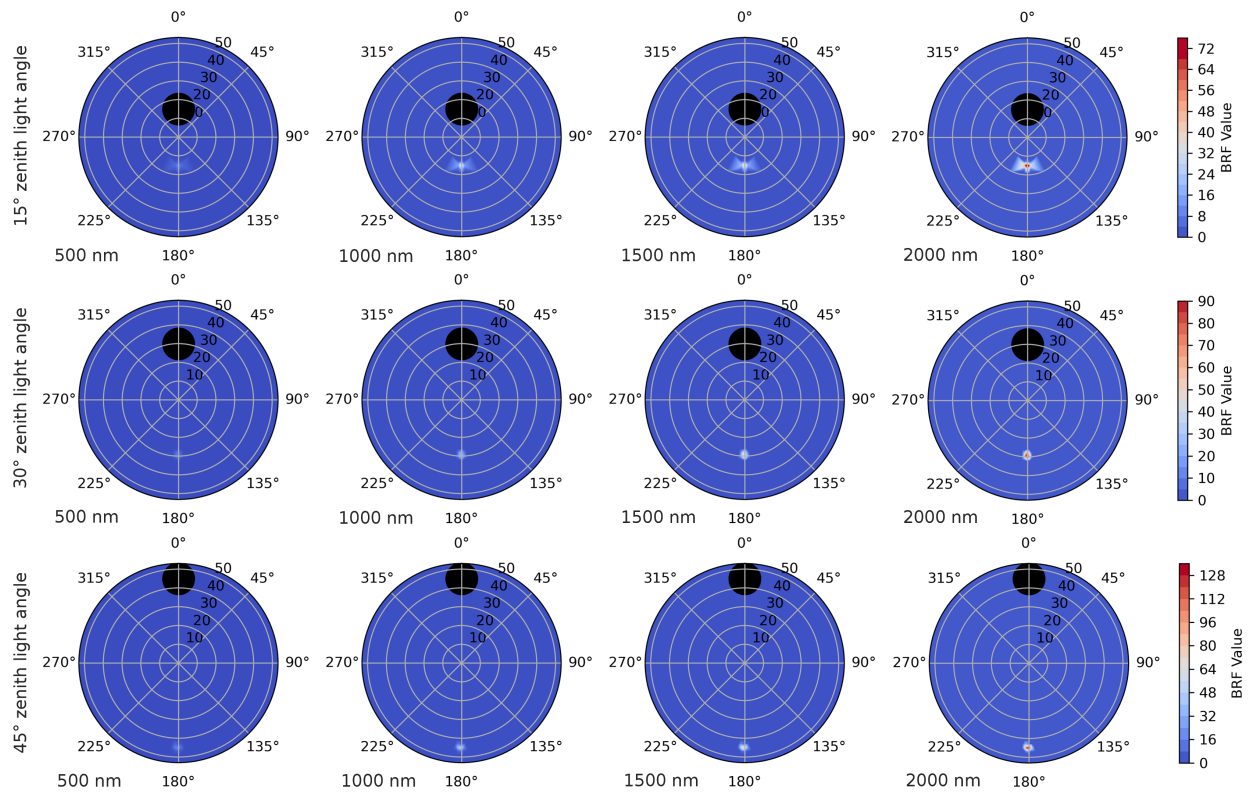
Fig. 6: BRFs of the middle photovoltaic cell on the CubeSat solar panel in a layout identical to that of Fig. 4. The winged appearance of the BRF at the specular region for the 15° illumination zenith angle measurements is likely an artifact from interpolating the BRFs.
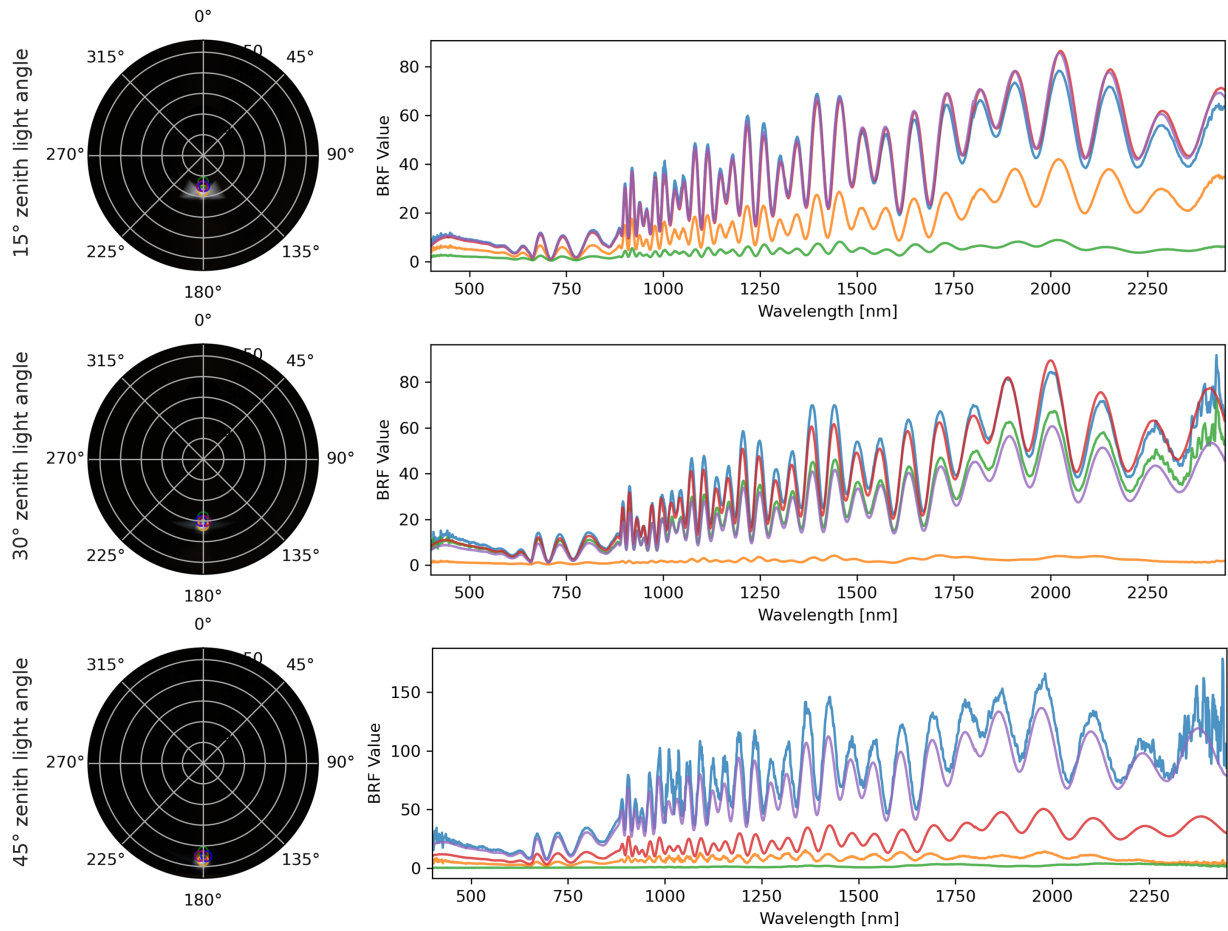
Fig. 7: Composite BRFs for a combination of single bands derived from the red, green, and blue portion of the measured spectrum of the middle photovoltaic cell on the CubeSat solar panel and individual spectra are shown in a layout identical to that of Fig. 5. The interference effects show various superimposed waves of multiple frequencies due to the numerous transmissive thin layers that comprise the photovoltaic cell.
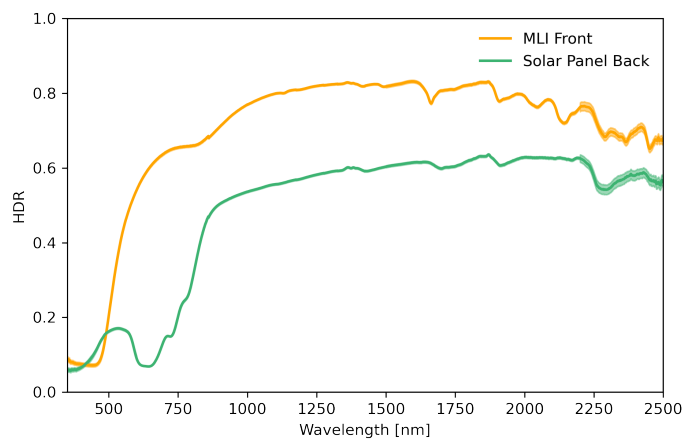

Fig. 8: HDR measurements of the front outer layer of the MLI and the back of the green solar panel board approximately color-coded to their apparent colors.

due to the reflected illumination being spread over more of the hemisphere from the wrinkled surface of the MLI. We also note that the 45° MLI BRF shows two broad peaks centered around two regions in the principal plane likely due to the measurement area including two skewed surfaces for this sequence.

The individual spectra from the BRFs of both materials show interference effects of varying degrees. The MLI spectra exhibit interference effects predominantly from a single frequency as a result of the single outer Kapton layer. In comparison, interference effects of various frequencies are present in the spectra of the photovoltaic cell as a result of its various thin transmissive layers. The thicknesses of these various layers in the solar cell and MLI could be retrieved by Fourier transforming the measured spectra.

The HDR of the MLI in Fig. 8 shows a similar spectral shape compared to the BRF spectra, but its interference effects are not present which we hypothesize is due to the interference effects averaging out when the sample is diffusely illuminated. The BRF of the MLI spectra show that the phases of the interference effects are not aligned with each other. Under diffuse illumination, the interference effects would average out, resulting in the spectrum shown.

The polarization ratio spectra derived from the Headwall imaging system and linear polarizer appear in Fig. 9. These spectra show that the ratio values depend on both shape and measurement wavelength of the target. For the MLI, the color-coded plots show that the brighter pixels, or the areas of the MLI that reflect the illumination in a more specular manner, have more positive ratio values in the distribution. In contrast, the darker pixels, or the areas of the MLI that are captured in a more oblique viewing geometry, have more negative ratio values in the distribution. As a result, the brighter pixels have a shallower negative polarization branch compared to that of darker pixels. The polarization ratio spectra for the green solar panel board and photovoltaic cell have different distributions, although the low signal from the solar cells caused a large spread in the observed spectra for those spectra with negative ratio values.

Our future work will include measurements for a variety of MLI samples of different compositions with various substrate layers. We plan to measure their spectral directional reflectances in various modes, such as in rough and smooth surface states with different substrate layers to compare and contrast their directional reflectance spectroscopy.
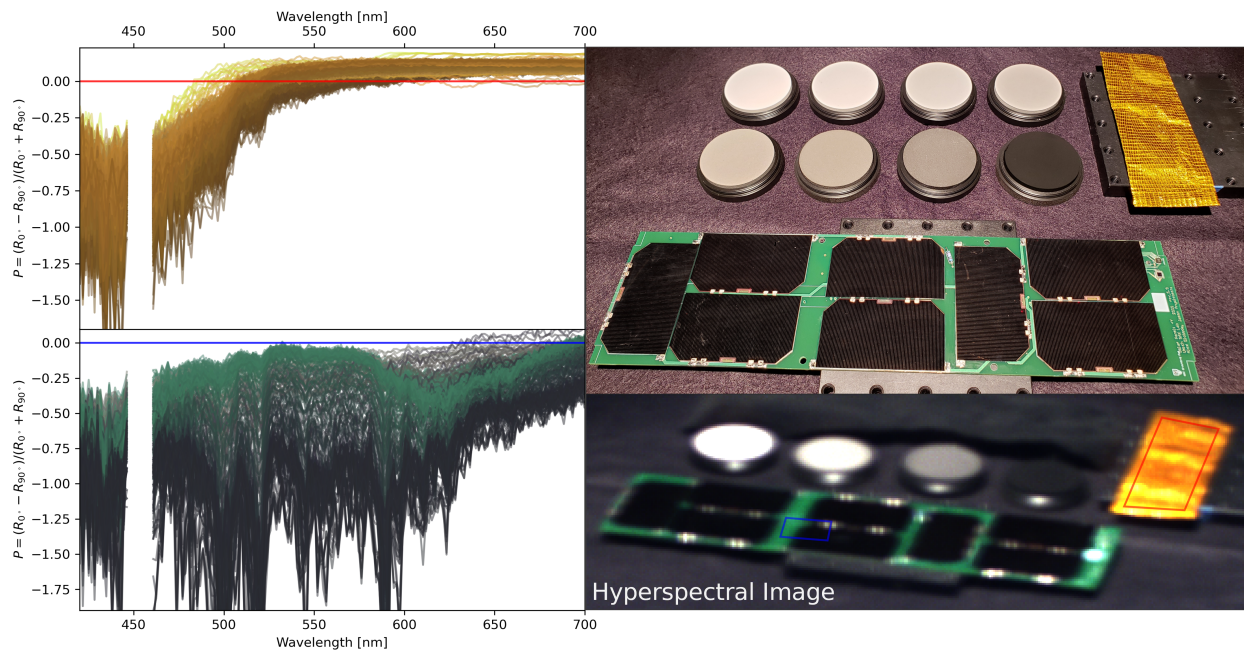
Fig. 9: Results from the spectral polarimetry measurements with the Headwall imaging system are shown, where the polarization ratio spectra are calculated as defined in Eq. 3. Each individual spectrum in the plots is color-coded to its perceived visible color. (Top left) The distribution of polarization ratio spectra for the region of interest on the MLI as defined by the red polygon superimposed on the HSI frame in the bottom right. (Bottom left) Similarly, the distribution of polarization ratio spectra for the region of interest on the solar panel as defined by the blue polygon superimposed on the HSI frame. (Top right) A high-resolution picture of the measurement setup. (Bottom right) An unpolarized HSI taken in the same measurement configuration as the polarized measurements for reference. Measurements around the 450 nm bands were omitted due to low signal-to-noise ratio in our polarized calibration data.

4. CONCLUSION

We measured the spectral bi-directional reflectance factor (BRF), the spectral hemispherical directional reflectance (HDR), and polarization ratio spectra of a sample of aluminized Kapton multi-layer insulation (MLI) and a CubeSat solar panel with integrated Emcore BTJM photovolatic cells. These measurements were taken primarily using the Goniometer of the Rochester Institute of Technology-Two (GRIT-T) [8], a small LabSphere integrating sphere, and a Headwall Photonics micro-HE imaging spectrometer with an attachable linear polarizer. Interference effects of varying degrees were observed in the BRF spectra according to the thinly layered composition of the materials, and the HDR of the MLI showed an absence of interference phenomena due to the diffuse illumination averaging out the interference effects in the nadir directional measurement. The polarization ratio spectra showed its dependence on the shape and material composition of the samples and the measured wavelength of light.

REFERENCES

[1] C. M. Bachmann, R. S. Eon, C. S. Lapszynski, G. P. Badura, A. Vodacek, M. J. Hoffman, D. McKeown, R. L. Kremens, M. Richardson, T. Bauch, and M. Foote, "A low-rate video approach to hyperspectral imaging of dynamic scenes," *Journal of Imaging*, vol. 5, no. 1, 2019. [Online]. Available: https://www.mdpi.com/2313-433X/5/1/6

[2] R. Eon, C. Bachmann, C. Lapszynski, A. Tyler, and S. Goldsmith, "Retrieval of sediment filling factor in a salt panne from multi-view hyperspectral imagery," *Remote Sensing*, vol. 12, p. 422, 01 2020.

[3] G. Badura, E. Plis, and C. R. Valenta, "Extending laboratory brdf measurements towards radiometric modeling of resident space object spectral signature mixing," in *2021 AMOS Conference Proceedings*, 2021.

[4] J. Hostetler and H. Cowardin, "Experimentally-derived bidirectional reflectance distribution function data in support of the orbital debris program office," in *2019 AMOS Conference Proceedings*, 2019.

[5] F. E. Nicodemus, J. C. Richmond, J. J. Hsia, I. W. Ginsberg, and T. Limperis, "Geometrical considerations and nomenclature for reflectance," 1977.

[6] B. Hapke, *Theory of Reflectance and Emittance Spectroscopy*. Cambridge University Press, 2012.

[7] M. Levesque and M. Dissanska, "Correction of the calibration measurement by taking into account the spectralon(tm) spectro-polarimetric brdf model," 09 2018, p. 18.

[8] J. D. Harms, C. M. Bachmann, B. L. Ambeau, J. W. Faulring, A. J. R. Torres, G. Badura, and E. Myers, "Fully automated laboratory and field-portable goniometer used for performing accurate and precise multiangular reflectance measurements," *Journal of Applied Remote Sensing*, vol. 11, no. 4, pp. 046 014–15, 2017. [Online]. Available: https://dx.doi.org/10.1117/1.JRS.11.046014

[9] L. Zimmerman, S. Chun, M. Pirozzoli, M. Plummer, F. Chun, and D. Strong, "Near- simultaneous polarization and spectral optical measurements of geosynchronous satellites," in *2020 AMOS Conference Proceedings*, 2020.

[10] J. Kurtz, A. Jolley, and S. Tyo, "Light scattering properties of a solar panel including wavelength and polarization dependencies in the visible spectrum," in *2021 AMOS Conference Proceedings*, 2021.

[11] C. M. Bachmann, R. S. Eon, B. Ambeau, J. Harms, G. Badura, and C. Griffo, "Modeling and intercomparison of field and laboratory hyperspectral goniometer measurements with G-LiHT imagery of the algodones dunes," *Journal of Applied Remote Sensing*, vol. 12, no. 1, p. 012005, 2017. [Online]. Available: https://dx.doi.org/10.1117/1.JRS.12.012005

[12] G. Badura and C. M. Bachmann, "Assessing effects of azimuthally oriented roughness on directional reflectance of sand," *IEEE Journal of Selected Topics in Applied Earth Observations and Remote Sensing*, vol. 12, no. 3, pp. 1012–1025, 2019. [Online]. Available: https://dx.doi.org/10.1109/JSTARS.2019.2896592

[13] G. Badura, C. M. Bachmann, J. Harms, and A. Abelev, "Observed relationship between brf spectral-continuum variance and macroscopic roughness of clay sediments," *IEEE Transactions on Geoscience and Remote Sensing*, vol. 57, no. 9, pp. 6726–6740, 2019. [Online]. Available: https://dx.doi.org/10.1109/TGRS.2019.2908170

[14] G. P. Badura, C. M. Bachmann, A. C. Tyler, S. Goldsmith, R. S. R. S. Eon, and C. S. Lapszynski, "A novel approach for deriving lai of salt marsh vegetation using structure from motion and multiangular spectra," *IEEE Journal of Selected Topics in Applied Earth Observations and Remote Sensing*, vol. 12, no. 2, pp. 599–613, 2019. [Online]. Available: https://dx.doi.org/10.1109/JSTARS.2018.2889476

[15] B. D. Roth, M. G. Saunders, C. M. Bachmann, and J. A. van Aardt, "On leaf brdf estimates and their fit to microfacet models," *IEEE Journal of Selected Topics in Applied Earth Observations and Remote Sensing*, vol. 13,

pp. 1761–1771, 2020.

[16] B. Roth, M. G. Saunders, C. M. Bachmann, and J. van Aardt, "On leaf bidirectional transmittance distribution function (btdf) estimates and their extension to a microfacet model," *IEEE Transactions on Geoscience and Remote Sensing*, p. in press.

[17] R. S. Eon and C. M. Bachmann, "Mapping barrier island soil moisture using a radiative transfer model of hyperspectral imagery from an unmanned aerial system," *Scientific Reports*, vol. 11, no. 3270, 2021. [Online]. Available: https://www.nature.com/articles/s41598-021-82783-3